Catalysis Science & Technology

ROYAL SOCIETY OF CHEMISTRY

PAPER

View Article Online
View Journal | View Issue

Check for updates

Cite this: *Catal. Sci. Technol.*, 2024, 14, 379

Reversible transformation of sub-nanometer Ga-based clusters to isolated $^{[4]}Ga_{(4Si)}$ sites creates active centers for propane dehydrogenation†

Zixuan Chen, [a] Alexander I. Serykh, [b] Agnieszka Kierzkowska, [a] David Gajan,[c] Scott R. Docherty,[d] Alexander V. Yakimov,[d] Paula M. Abdala, [a] Christophe Copéret, [d] Pierre Florian, *[e] Alexey Fedorov *[a] and Christoph R. Müller *[a]

Ga-based propane dehydrogenation (PDH) catalysts are explored in industry as an alternative to PtSn and CrO_x-based catalysts. Yet, at present, there is only limited understanding of the structural dynamics of surface sites in Ga-based PDH catalysts. Here, we employ atomic layer deposition (ALD) to engineer a sub-monolayer of Ga species on dehydroxylated silica, which serves as a model PDH catalyst. While the ALD-grown shell contains, after calcination at 500 °C, tetra- and pentacoordinate Ga^{3+} sites with both Si and Ga atoms in the second coordination sphere (*i.e.*, $^{[4]}Ga_{(Si/Ga)}$ and $^{[5]}Ga_{(Si/Ga)}$ sites), its exposure to ambient air leads to sub-nanometer $Ga_xO_y(OH)_z$ clusters with $^{[4]}Ga_{(Ga)}$ and $^{[6]}Ga_{(Ga)}$ sites, due to the hydrolysis of the Ga–O–Si linkages by the moisture of ambient air. When calcining the material at 650 °C, the $^{[4]}Ga_{(Ga)}$ and $^{[6]}Ga_{(Ga)}$ sites evolve leading to a silica surface dominated by isolated tetracoordinate $^{[4]}Ga_{(4Si)}$ sites, that is, $[(\equiv SiO)_3Ga(XO Si\equiv)]$ sites, where X is H or $\equiv Si$. Exposure of the dehydroxylated material with $^{[4]}Ga_{(4Si)}$ sites to ambient air reforms the sub-nanometer $Ga_xO_y(OH)_z$ clusters, indicating the reversibility of the Ga dispersion and agglomeration as a function of the extent of silica (de)hydroxylation. The presence of $^{[4]}Ga_{(4Si)}$ sites coincides with a high performance in PDH, achieving an initial turnover frequency of *ca.* 12 h^{-1} and propene selectivity of *ca.* 85%, while deactivating by only 34% over 20 h of time on stream. Overall, our results highlight the dynamic nature of the dispersion and agglomeration of Ga^{3+} sites during the dehydroxylation (by calcination) and rehydration (ambient air exposure).

Received 17th October 2023,
Accepted 23rd November 2023

DOI: 10.1039/d3cy01446k

rsc.li/catalysis

Introduction

Propene is an essential platform chemical with an unmet demand, mostly due to its growing use as a monomer in the production of plastics (polypropylene).[1,2] In this context, the on-purpose production of propene, for instance, *via* propane dehydrogenation (PDH), has emerged as a viable strategy to mitigate the increasing gap between production and demand.[3,4] While various catalysts based on Pt or Cr have been developed for the industrial production of propene *via* PDH, the most recent development has focused on the introduction of Ga to Pt-based catalysts.[5–8] These works have led to a $PtGa/Al_2O_3$ catalyst utilized in the fluidized catalytic dehydrogenation (FCDh) technology that currently undergoes industrial implementation.[9,10] Highly dispersed Ga sites on silica (in the absence of Pt) have also been shown to catalyze PDH.[11–13] In previous studies, a material ($Ga@SiO_2$) with isolated $^{[4]}Ga_{(4Si)}$ sites, *i.e.*, $[(\equiv SiO)_3Ga(XO Si\equiv)]$ (where X is H or $\equiv Si$),[11] was generated using surface organometallic chemistry (SOMC),[14,15] and a thermolytic molecular precursor approach.[16] $Ga@SiO_2$ displayed high activity, selectivity and stability for propane dehydrogenation.[11]

An alternative, less explored strategy to generate isolated sites is atomic layer deposition (ALD), which is more commonly used to grow thin films.[17–20] In our recent work, targeting at understanding the structure and surface properties of Ga-based films generated on a dehydroxylated silica support, we have observed that the deposition of one ALD cycle of trimethylgallium followed by calcination at 500 °C yields a submonolayer coverage of tetracoordinate and pentacoordinate Ga^{3+} sites that contain, in their second

[a] *Department of Mechanical and Process Engineering, ETH Zürich, Switzerland. E-mail: fedoroal@ethz.ch, muelchri@ethz.ch*
[b] *Zelinsky Institute of Organic Chemistry, RAS, Moscow, Russia*
[c] *Centre de RMN à hauts champs de Lyon, UMR 5082 (CNRS, ENS Lyon, Université Lyon 1), Université de Lyon, Villeurbanne F-69100, France*
[d] *Department of Chemistry and Applied Biosciences, ETH Zürich, Switzerland*
[e] *CNRS, CEMHTI UPR3079, Université d'Orléans, France. E-mail: pierre.florian@cnrs-orleans.fr*

† Electronic supplementary information (ESI) available. See DOI: https://doi.org/10.1039/d3cy01446k

coordination sphere, both Si and Ga atoms (that is, $^{[4]}Ga_{(Si/Ga)}$ and $^{[5]}Ga_{(Si/Ga)}$, respectively).[21] Interestingly, $^{[4]}Ga_{(Si/Ga)}$ sites provide strong Lewis acidity and their higher relative amount correlates with a higher activity in isobutane dehydrogenation. That being said, materials obtained using five and ten ALD cycles show a higher relative fraction of $^{[5]}Ga_{(Si/Ga)}$ sites that are associated with mild Lewis acidity and are also less active in isobutane dehydrogenation and produce more coke. In contrast, the more active sites in unsupported nanoparticle catalysts such as β-Ga_2O_3 or mixed oxide $(Ga,Al)_2O_3$ are weak Lewis acid sites (LAS), yet a higher relative amount of mild LAS in those catalysts also leads to increased amounts of coking.[22–25]

Here, we report that ALD-made $^{[4]}Ga_{(Si/Ga)}$ and $^{[5]}Ga_{(Si/Ga)}$ sites on dehydroxylated silica transform, upon contact with ambient air, to $^{[4]}Ga_{(Ga)}$ and $^{[6]}Ga_{(Ga)}$ sites that are contained in *ca.* sub-nanometer $Ga_xO_y(OH)_z$ clusters that feature no diffraction peaks and are not-discernable by high-resolution TEM.[21] Calcination at 650 °C leads to their conversion into $^{[4]}Ga_{(4Si)}$ sites that are similar (both structurally and catalytically) to the isolated sites that are obtained by SOMC, *i.e.*, $[(\equiv SiO)_3Ga(XOSi\equiv)]$ sites (one strong LAS and one strong BAS). Interestingly, exposure of the dehydroxylated material containing $^{[4]}Ga_{(4Si)}$ sites to ambient air regenerates the $^{[4]}Ga_{(Ga)}$ and $^{[6]}Ga_{(Ga)}$ sites in $Ga_xO_y(OH)_z$ clusters (Scheme 1). Thus, the transformation of isolated $^{[4]}$-$Ga_{(4Si)}$ sites to agglomerated $^{[4,6]}Ga_{(Ga)}$ sites contained in sub-nanometer $Ga_xO_y(OH)_z$ clusters (shells) is reversible and can be tuned dynamically as a function of the extent of silica dehydroxylation, which in turn is controlled by the pretreatment temperature.

Experimental section

Materials

Ga1–SiO_{2-500} was synthesized using a previously reported method (*vide infra*),[21] and is denoted hereafter as $Ga1_{(500)}$. Exposure of $Ga1_{(500)}$ to ambient air gave a material denoted as $Ga1_{(500\text{-air})}$. Calcination of $Ga1_{(500)}$ in synthetic air at 650 °C for 1 h (20 ml min^{-1}, 5 °C min^{-1}) produced a material denoted as $Ga1_{(650)}$ that was handled and stored without exposure to air. We also refer to a material obtained from $Ga1_{(500\text{-air})}$ under similar conditions during an *in situ* X-ray absorption spectroscopy (XAS) experiment as $Ga1_{(650)}$. Lastly, we refer to the materials obtained after vacuum treatment of $Ga1_{(500\text{-air})}$ at 550 °C and 650 °C during FTIR experiments as $Ga1_{(550)}$ and $Ga1_{(650)}$, respectively. A reference material Ga@SiO_2 (containing $[(\equiv SiO)_3Ga(XOSi\equiv)]$ sites) was prepared using SOMC/TMP, utilizing $[Ga(OSi(O^tBu)_3)_3(THF)]$ as the organometallic precursor, as described previously.[11] Exposure of $Ga1_{(650)}$ to ambient air gave a material denoted as $Ga1_{(650\text{-air})}$.

Atomic layer deposition

The deposition of trimethylgallium (TMG, Pegasus Chemicals) onto silica, dehydroxylated at 500 °C (SiO_{2-500}), and using ozone as an oxidant was performed at 300 °C in a Picosun R-200 system enclosed within an MBraun glovebox (H_2O, $O_2 < 1$ ppm). An ALD cycle included 20 pulses of TMG (0.1 s duration for each pulse) and 20 ozone pulses (5 s duration for each pulse). N_2 (99.999%) was used as the carrier and purge gas in the ALD experiments. The ozone concentration expected at the power used is 10% w/w (140 g Nm^{-3}). The resulting material was calcined, without exposure to ambient air, at 500 °C in a flow of synthetic air for 4 h (flow rate was 50 ml min^{-1}, heating ramp was 5 °C min^{-1}) to yield $Ga1_{(500)}$ that was handled and stored in a glovebox (H_2O, $O_2 < 1$ ppm).[21]

Elemental analysis

The Ga wt% content was determined using inductively coupled plasma-optical emission spectroscopy (ICP-OES) using an Agilent 5100 VDV instrument, calibrated according to a multi-element standard. The materials were dissolved in *aqua regia* (3 : 1; HCl : HNO_3) and digested at 175 °C for 30 min in a microwave system (Multiwave GO). The resulting solutions were diluted using deionized water to match the linear range of the standard.

X-ray powder diffraction (XRD)

XRD data were obtained using a Panalytical Empyrean diffractometer with a Cu Kα radiation source set at 45 kV and 40 mA. The detector used was an ultrafast line X'Celerator

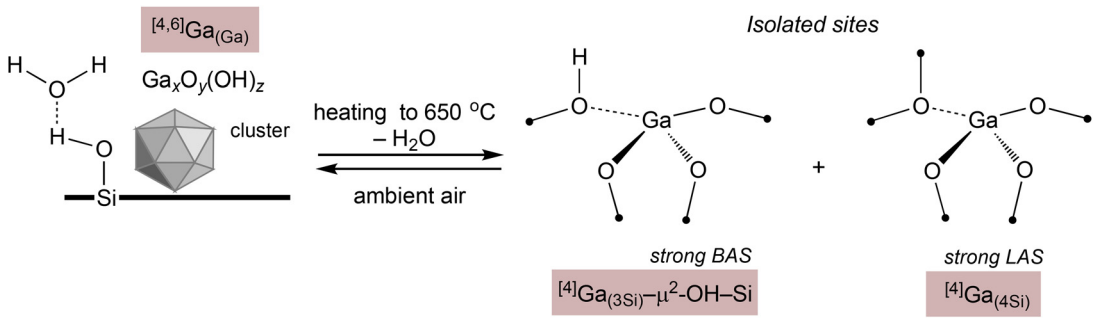

Scheme 1 Schematic representation of the structural changes occurring during the dehydroxylation of silica-supported sub-nanometer clusters of gallia ($Ga_xO_y(OH)_z$).

Scientific and the incident beam was equipped with a Bragg–Brentano HD optic. The diffractograms were acquired between 5 and 70° 2θ (the step size was 0.0167° using 0.4 s step^{-1} acquisition time).

Transmission electron microscopy (TEM)

The microstructure of the materials (opened to air) was probed by TEM (FEI Talos F200X) equipped with a high-brightness field-emission gun, a high-angle annular dark field (HAADF) detector, and a large collection-angle EDX detector. The operation voltage of the instrument was set to 200 kV in scanning transmission electron microscopy (STEM) mode. The specimens for electron microscopy were prepared by dipping the Cu grids coated with carbon (TedPella, 300 mesh) into the powder.

Ga K-edge X-ray absorption spectroscopy

XAS measurements were performed at the BM31 station of the Swiss-Norwegian beamlines (SNBL) at the European Synchrotron Radiation Facility (ESRF). Data collection was carried out at the Ga K-edge using continuous scanning in transmission mode with a double-crystal Si(111) monochromator. *In situ* XAS experiments were carried out in a quartz capillary reactor (diameter 1 mm; wall thickness = 0.1 mm) whereby the material was placed between two quartz wool plugs. The material was subjected to a dehydroxylation treatment by flowing synthetic air (10 mL min^{-1}) through the reactor while heating the material from room temperature to 650 °C (5 °C min^{-1}) using an air blower. The material was kept at 650 °C for 1 h and then cooled down while the reactor was flushed with N_2 (10 mL min^{-1}). For *ex situ* XAS measurements, materials were placed inside quartz capillaries (diameter 1.5 mm; wall thickness 0.1 mm) and sealed with wax and vacuum grease inside a N_2-filled glovebox (H_2O, $O_2 < 1$ ppm). All *ex situ* measurements were conducted at room temperature.

The Demeter software was used for data processing. The spectral energy was calibrated using a Zn foil (9659 eV). Extended X-ray absorption fine structure (EXAFS) data were fitted in R space between 1 and 3.0 Å with a k-weight of 3. The Fourier transform (FT) of the EXAFS oscillations was obtained for a k-space range of 3–11 Å^{-1}. The initial FEFF paths (Ga–O and Ga–Ga) and the amplitude reduction factor (S_0^2) were generated by the Artemis software using β-Ga_2O_3 as the reference model.

The continuous Cauchy wavelet transform (CCWT) analysis was performed with MATLAB software using an open script downloaded from **http://www.univ-mlv.fr/~farges/waw**.[26] The Cauchy order was set to 20 while analyzing the long-range EXAFS data in R space from 0.5 to 4 Å. To yield a better resolution of the CCWT images, we increased the Cauchy order to 150 for short-range R space (2–4 Å) analysis.

^{71}Ga NMR

^{71}Ga magic angle spinning nuclear magnetic resonance (MAS NMR) experiments were performed using a 20.0 T Bruker Neo spectrometer operating at a frequency of 259.3 MHz. Materials were packed into 1.3 mm diameter zirconia rotors inside an argon-filled glovebox. The rotors were spun at 60 kHz under pure nitrogen. In order to increase the signal-to-noise ratio, the signal acquisition has been performed with a Carr–Purcell–Meiboom–Gill (CPMG) pulse sequence,[27] co-adding 64 to 128 echoes separated by approx. 40 μs to 125 μs (*i.e.*, 2 to 8 rotor periods) and using radio-frequency fields set at 150 kHz with an optimized t_{90} pulse duration of 0.6 μs and a recycle delay of 0.5 s. Reducing the pulse length below 0.6 μs did not change significantly the line shape, showing that those irradiation conditions did not produce any significant pulse bandwidth issues. Depending on the material studied, the total experimental times were ranging typically between 15 h and 48 h. Further experiments were performed on a 23.8 T Bruker Neo spectrometer operating at a frequency of 305.0 MHz using identical experimental conditions, except for slight changes in the CPMG pulse length (0.7 μs was found to be optimal and using 200 echos, except for $Ga1_{(500\text{-air})}$ and $Ga1_{(650\text{-air})}$ that showed a much shorter apparent T_2 relaxation time). Chemical shifts were referenced to a 1 M solution of $Ga(NO_3)_3$ in H_2O (for both fields).

Simulations were performed using the Czjzek model, as further developed and implemented in the DMFit software,[28] *i.e.*, the so-called Gaussian isotropic model (GIM) was used under the assumption of a finite spinning speed, that is, taking into account the spinning sidebands of the central transition arising from the second-order quadrupolar effects.[29] This approach allows us to differentiate the individual components and to retrieve the relevant spectroscopic parameters, *i.e.*, the mean isotropic chemical shift $\bar{\delta}_{iso}$, the width of its Gaussian distribution $\Delta\delta_{iso}$, the variance of the distribution of the quadrupolar tensor elements (σ_Q) and the relative fraction of each component. Worthy of note, this model assumes a random distribution of structural environments such that σ_Q and $\Delta\delta_{iso}$ become solely a measure of extent of disorder in the material studied.

Fourier-transform infrared spectroscopy (FTIR)

FTIR spectra were recorded on a Nicolet Protege 360 spectrophotometer in transmittance mode (spectral resolution 4 cm^{-1}). Powdered materials were pressed into self-supporting wafers (15–20 mg cm^{-2}) and placed into a vacuum infrared quartz cell equipped with CaF_2 windows. For the dehydroxylation process, $Ga1_{(500\text{-air})}$ was heated in vacuum (*ca.* 10^{-5} mbar) at a rate of 3 °C min^{-1} and held for 3 h at a desired temperature. All IR spectra were measured at room temperature. $Ga1_{(500\text{-air})}$, dehydroxylated at different temperatures was also characterized after adsorption of CO. The adsorption of CO was conducted at room temperature and using an equilibrium pressure of *ca.* 20 Torr. For the H_2 dissociation experiments, the materials were outgassed at 650 °C for 2 h under a vacuum of *ca.* 10^{-5} mbar. Subsequently, hydrogen was introduced at a pressure of 50

Torr (*ca.* 67 mbar) and held for one minute after which the reactor containing the self-supporting specimen pellet was removed from the oven, allowed to cool down to room temperature and then outgassed.

Determination of surface acidity with pyridine

^{15}N-Pyridine (99% isotopic enrichment) was purchased from CortecNet Corp., dried over CaH_2 at 60 °C for 2 days and degassed by three freeze-pump-thaw cycles prior to use. The materials were evacuated (*ca.* 10^{-5} mbar) and then exposed to vapor of ^{15}N-Py at ambient temperature for 1 min followed by outgassing (150 °C, 5 °C min^{-1}, *ca.* 10^{-5} mbar). The FTIR spectra of the outgassed specimen were collected using an Alpha II spectrometer (Bruker) operated inside a N_2 filled glovebox using self-supporting pellets.

For ^{15}N dynamic nuclear polarization surface enhanced NMR spectroscopy (DNP SENS) measurements, materials with pre-adsorbed Py were impregnated in a glovebox (O_2 and H_2O < 0.5 ppm) with a 16 mM TEKPol in 1,1,2,2-tetrachloroethane (TCE) solution. The impregnated materials were introduced into a sapphire rotor (outer diameter 3.2 mm), and closed with a zirconia cap. The rotor was placed quickly in a cold DNP probe (109 K). The measurements were performed on a Bruker 600 MHz (14.1 T) instrument equipped with a 3.2 mm Bruker DNP triple-resonance probe coupled to a 395 GHz gyrotron microwave source (output power = 6–10 W) to drive the DNP cross-effect. In all experiments, a MAS rate of 8 kHz was used. DNP-enhanced ^{15}N NMR spectra were measured using a $[^1H]^{15}N$ CPMAS pulse sequence using a contact time of 2 ms. As a reference for the static magnetic field, the higher-frequency ^{13}C peak of adamantane at 38.4 ppm was used. The DNP buildup time (τ_{DNP}) was measured by a ^{1}H saturation-recovery experiment with the microwaves turned on.

Catalytic testing

Propane dehydrogenation tests were carried out in a benchtop Microactivity EFFI reactor (PID Eng&Tech). Typically, 50 mg of a catalyst was diluted with 1.5 g of SiC (46 grit, Alfa-Aesar) and placed between two plugs of quartz wool on a quartz frit in a 13 mm ID quartz reactor. The catalyst was loaded and sealed inside a N_2 glovebox and purged with N_2 using a bypass prior to the catalytic test. After reaching the desired reaction temperature (550 °C, 10 °C min^{-1}), during heating in a N_2 flow (20 ml min^{-1}), a mixture of 10% C_3H_8 diluted in N_2 was introduced to the reactor using a weight hourly space velocity (WHSV) of 8.5 h^{-1}. The gas flow rates were controlled by mass flow controllers, which were calibrated to the desired gases. The temperature was controlled by a thermocouple immersed inside the catalyst bed. The composition of the outlet gases was analyzed by a 4-channel compact gas chromatography system (CompactGC 4.0, Global Analyser Solutions) equipped with two thermal conductivity detectors (TCD) and two flame ionization detectors (FID). The data points were collected every 7 min. To assess the activity of the catalysts after reoxidation, a regeneration step was incorporated every 5 h of time-on-stream. The regeneration step involved the flowing of synthetic air (30 mL min^{-1} at 550 °C, obtained by mixing dry N_2 and dry O_2) for 1 h, followed by a flushing step with N_2 (20 min, 30 mL min^{-1}) before starting a new PDH cycle.

The fractions of the gas-phase products ($C_{x,out}$) were determined by calibrating the GC with a gas mixture of known fractions. The formation rate of products ($F_{x,out}$, mol min^{-1}) was calculated based on the gas fractions measured in the outlet flow. The propane conversion ($X_{C_3H_8}$) and the selectivity of the gas-phase products (S_x, defined per mole of product) were calculated based on the following equations:

$$F_{x,out}\left[\text{mol min}^{-1}\right] = \frac{C_{x,out} F_{N_2,in}}{C_{N_2,out}}$$

$$X_{C_3H_8} = \frac{\sum F_{i,out}}{F_{C_3H_8,in}} \times 100\%$$

$$S_x = \frac{F_{x,out}}{\sum F_{i,out}}$$

$$\text{Carbon balance} = \frac{\sum F_{x,out} \times N_x + F_{C_3H_8,out} \times N_{C_3H_8}}{F_{C_3H_8,in} \times N_{C_3H_8}}$$

Results and discussion

Material synthesis and basic characterization

$Ga1_{(500)}$ was synthesized as reported previously, using one ALD cycle (300 °C deposition temperature) of trimethylgallium, ozone and silica partially dehydroxylated at 500 °C, *i.e.*, SiO_{2-500}, followed by calcination in synthetic air at 500 °C for 4 h.[21] Exposure of $Ga1_{(500)}$ to ambient air gave the material denoted as $Ga1_{(500\text{-air})}$. Calcination and/or dehydroxylation (in FTIR experiments) of $Ga1_{(500\text{-air})}$ at 650 °C gave the materials denoted as $Ga1_{(650)}$ or $Ga1_{(650\text{-air})}$, if exposed to air (Scheme 2). ICP-OES analysis shows that the Ga loading in $Ga1_{(650\text{-air})}$ is 5.1 wt%. In addition, N_2 physisorption measurement gives a BET specific surface area of $Ga1_{(650\text{-air})}$ of 178 m^2 g^{-1}. The pore volume of $Ga1_{(650\text{-air})}$ is 1.5 cm^3 g^{-1}. XRD data shows the absence of crystalline phases in $Ga1_{(650)}$, only amorphous halos due to diffuse scattering from silica are detected (Fig. S1†).

Catalytic performance

The catalytic performance of $Ga1_{(650)}$ in PDH was then evaluated using a flow of 10% C_3H_8/N_2 that was passed through a catalyst bed (50 mg of catalysts mixed with 1.5 g SiC) held at 550 °C using a WHSV of 8.5 h^{-1}. Initially (*i.e.*,

$$Ga1_{(500)} \xrightarrow[\text{air}]{\text{ambient}} Ga1_{(500\text{-air})} \xrightarrow[-H_2O]{\Delta\ (650\ ^\circ C)} Ga1_{(650)} \xrightarrow[\text{air}]{\text{ambient}} Ga1_{(650\text{-air})}$$

Scheme 2 Synthesis of the materials used in this work.

after 7 min), $Ga1_{(650)}$ exhibited a propene selectivity of 85.4%. The corresponding TOF (mol C_3H_6 per mol Ga per hour) was 11.7 h^{-1}, achieved at 8.0% propane conversion (Fig. 1a). In comparison, the previously reported SOMC-derived $Ga@SiO_2$ catalyst containing isolated $^{[4]}Ga_{(4Si)}$ sites exhibited an initial TOF of 20.4 h^{-1}, although obtained at a significantly lower WHSV of 2.1 h^{-1}.[11] Importantly, the propene selectivity and deactivation profiles are comparable in these two catalysts. Over 20 h of time on stream, the catalyst's selectivity to propene decreased slightly to 80%, while the TOF decreased to 7.7 h^{-1} (at 5.5% propane conversion). A possible reason for the observed deactivation with time on stream is the partial reduction of the active $^{[4]}Ga_{(4Si)}$ sites, as has been reported for the SOMC-derived $Ga@SiO_2$ catalyst.[11] The formation rates of methane and ethene (cracking byproducts), remained constant with time on stream (Fig. S14†), which may be due to different active sites for PDH and cracking reactions. After 20 h of time on stream, there was only a slight darkening of the catalyst, suggesting a minor degree of coke deposition and a limited contribution of coking to catalyst deactivation. Previously, mild LAS have been suggested to be linked to coking in alkane dehydrogenation,[21,23] and this hypothesis is generally consistent with only a limited degree of coking observed for $Ga1_{(650)}$ that lacks mild LAS (*vide infra*). The reaction–regeneration cycle was carried out on $Ga1_{(650)}$ by passing synthetic air at 550 °C for 1 h through the catalyst bed that has been exposed to PDH condition for 5 h. The PDH activity of $Ga1_{(650)}$ can be fully regenerated after oxidative treatment (and removal of minor amounts of coke) *via* calcination (Fig. S15†).

H_2 dissociation sites

Given the similarity between the catalytic results of $Ga1_{(650)}$ and the SOMC-prepared material $Ga@SiO_2$, we evaluated and monitored by IR spectroscopy the reactivity of these two materials towards H_2. To minimize the reduction of the dehydroxylated materials, we carried out the dissociation of H_2 at 300 °C (for 1 min, followed by cooling down under H_2 and outgassing at room temperature). Dissociation of H_2 on $Ga1_{(650)}$ results in the emergence of a rather narrow IR band centered at 2039 cm^{-1}, attributed to a Ga–H vibration (Fig. 1b). Importantly, the dissociation of H_2 on $Ga@SiO_{2(650)}$ yields the same major band, albeit with slightly more pronounced shoulders at 2062 cm^{-1} and 2074 cm^{-1}. The presence of these shoulders in $Ga@SiO_{2(650)}$ is likely due to slightly different experimental conditions and the ease of reduction of $^{[4]}Ga_{(4Si)}$ sites at 300 °C (and not due to the higher site homogeneity in $Ga1_{(650)}$). This comparison highlights the similarity of the hydrogen dissociation sites in $Ga1_{(650)}$ and $Ga@SiO_{2(650)}$ (and, presumably, the active sites in propane dehydrogenation). We note that the Ga–H bands in silica-supported crystalline (γ/β) or amorphous gallia are

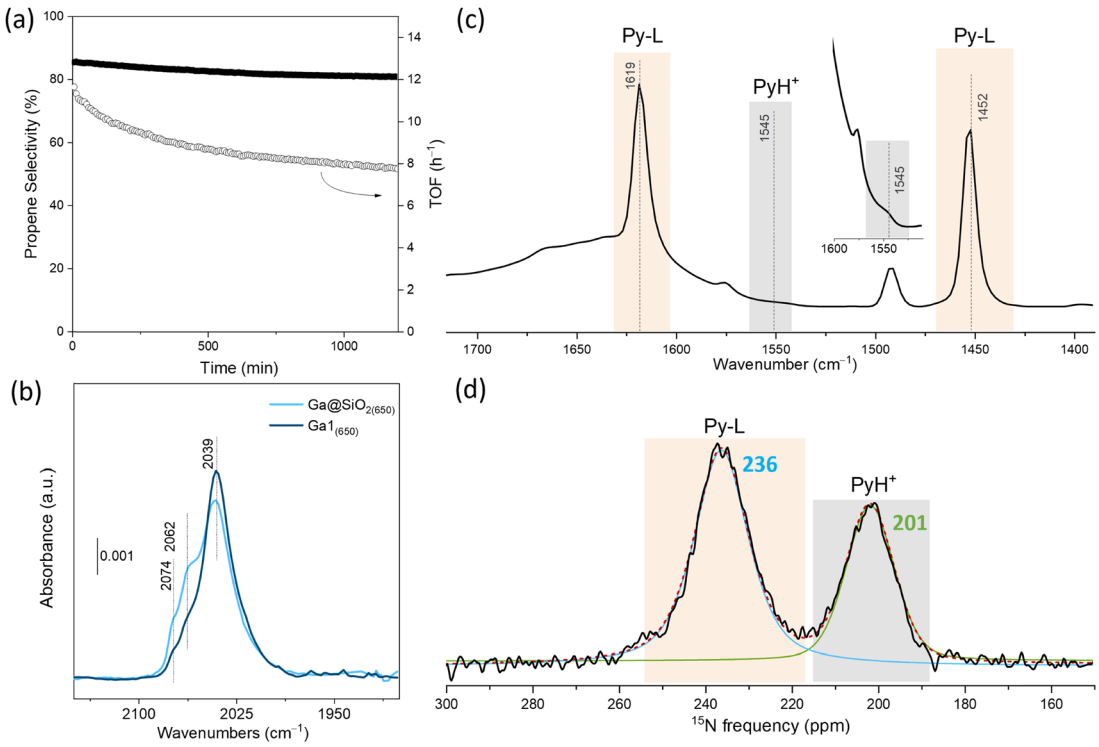

Fig. 1 (a) Propene selectivity and turn over frequency of $Ga1_{(650)}$ in propane dehydrogenation at 550 °C (20 h) with conversions in the range of 8.0–5.5% (WHSV = 8.5 h^{-1}). (b) Transmission FTIR results of H_2 dissociation experiments using the materials Ga1 and $Ga@SiO_2$ (navy and light blue, respectively) dehydroxylated at 650 °C, showing the region of the Ga–H bands. (c) FTIR spectra of Py–$Ga1_{(650)}$ after desorption of pyridine at 150 °C and (d) the corresponding fitted ^{15}N DNP SENS spectrum. Bands and peaks due to PyH^+ and Py–L are highlighted in grey and light peach, respectively. L indicates a Lewis acid site (such as $^{[4]}Ga_{(4Si)}$).

notably broader, and showing multiple bands in this region, consistent with a larger distribution of hydrogen dissociation sites in those materials.[24,30] As will be discussed in more detail below, the likely H_2 dissociation sites (and the active sites in PDH) in $Ga1_{(650)}$ and $Ga@SiO_{2(650)}$ are $^{[4]}Ga_{(4Si)}$ sites that split hydrogen heterolytically across the Ga–O bond, as has been proposed based on DFT calculations (the microscopic reverse of H_2 dissociation).[31]

Surface acidity by Py-FTIR and ^{15}N DNP SENS

The nature of surface acid sites in $Ga1_{(650)}$ was also further investigated using FTIR and ^{15}N DNP SENS using ^{15}N-Py as the probe molecule.[32,33] Fig. 1c displays the FTIR spectra of pyridine that remains adsorbed on the $Ga1_{(650)}$ surface after outgassing at 150 °C. Characteristic features associated with Py binding to LAS are evident at *ca.* 1619 cm^{-1} and 1452 cm^{-1}. The inset in Fig. 1c highlights the weak IR band at 1548 cm^{-1}, which corresponds to pyridinium. The ^{15}N DNP SENS spectrum for $Ga1_{(650)}$ after the desorption of ^{15}N-Py at 150 °C is presented in Fig. 1d. The spectrum reveals two distinct peaks located at isotropic ^{15}N chemical shifts at 236 ppm and 201 ppm. The 236 ppm signal is due to ^{15}N-Py's attachment to strong Lewis acidic Ga sites,[34] while the 201 ppm shift suggests the presence of pyridinium.[35,36] This latter signal indicates the existence of strong BAS, which are likely linked to pseudo-bridging silanols that interact with neighboring Ga sites, that is, $^{[4]}Ga_{(3Si)}$–μ^2-OH–Si. Note that the observed high sensitivity of ^{15}N DNP SENS to pyridinium, in contrast to Py-FTIR (Fig. 1c and d), is a general phenomenon when comparing the two methods.[21,23,24,37] ^{15}N DNP SENS is particularly sensitive for the detection of pyridinium because its nitrogen atom is directly bonded to a proton, which provides an increased NMR signal enhancement; performing the NMR measurement at low temperature further increases the signal-to-noise ratio and minimizes dynamic phenomena, which can impact the corresponding IR experiment (carried out at room temperature). Notably, the presence of only two peaks in the ^{15}N DNP SENS spectrum of $Ga1_{(650)}$ due to strong LAS and BAS parallels the spectrum of the SOMC-prepared $Ga@SiO_2$ material.[11,38] This similarity underscores that the majority of Ga centers on $Ga1_{(650)}$ are site-isolated, likely, tetracoordinate $^{[4]}Ga_{(4Si)}$ sites uniformly dispersed over the surface of dehydroxylated silica.

^{71}Ga MAS NMR study

A quantitative analysis of the local coordination of Ga sites in $Ga1_{(500\text{-air})}$, $Ga1_{(650)}$ and $Ga1_{(650\text{-air})}$ was performed using ^{71}Ga MAS NMR. In general, the nuclei of ^{71}Ga exhibit large quadrupolar interactions, leading to line broadening and a reduction of sensitivity, requiring in turn the use of fast magic angle spinning and high fields.[39] The spectrum of $Ga1_{(500\text{-air})}$ contains two peaks which can be well modeled at 20.0 T with a component with a $\bar{\delta}_{iso}$ at 186 ppm and a second component with a $\bar{\delta}_{iso}$ at 30 ppm, ascribed to $^{[4]}$Ga and $^{[6]}$Ga sites, respectively, similarly to β-Ga_2O_3 (Fig. 2a and S13,† Table 1).[40–42] In contrast, $Ga1_{(500)}$, described by us previously, contained no considerable amounts of $^{[6]}$Ga sites, but instead contained $^{[4]}$Ga and $^{[5]}$Ga sites with $\bar{\delta}_{iso}$ values at 176 ppm and 94 ppm at 20.0 T, respectively.[21] Both sites in $Ga1_{(500\text{-air})}$ can be modeled well with a Czjzek-type line shape but with significantly different values of σ_Q, *i.e.* 9.1 MHz for $^{[4]}$Ga and 4.9 MHz for $^{[6]}$Ga. The lower value found for $^{[6]}$Ga indicates that this environment is less disordered, possibly because of the presence of OH groups which restructure the Ga sites, as seen for Al sites in alumina.[43] Therefore, the presence of such $^{[6]}$Ga sites in $Ga1_{(500\text{-air})}$ suggests that the dispersed gallosilicate sites in dehydroxylated $Ga1_{(500)}$ transitioned into clusters of $Ga_xO_y(OH)_z$ upon exposing $Ga1_{(500)}$ to air, likely, *via* the hydrolysis of Si–O–Ga linkages. The resulting $Ga_xO_y(OH)_z$ clusters are too small to be observed by TEM or XRD.[21,44,45]

The spectrum of $Ga1_{(650)}$ exhibits significant peak broadening with the presence of numerous intense spinning sidebands. The simulation performed using a single Czjzek-type model accounts reasonably well (yet not perfectly) for this line shape, giving at 20.0 T (Fig. 2b) an average isotropic chemical shift $\bar{\delta}_{iso}$ of 155 ppm (138 ppm at 23.5 T) with a

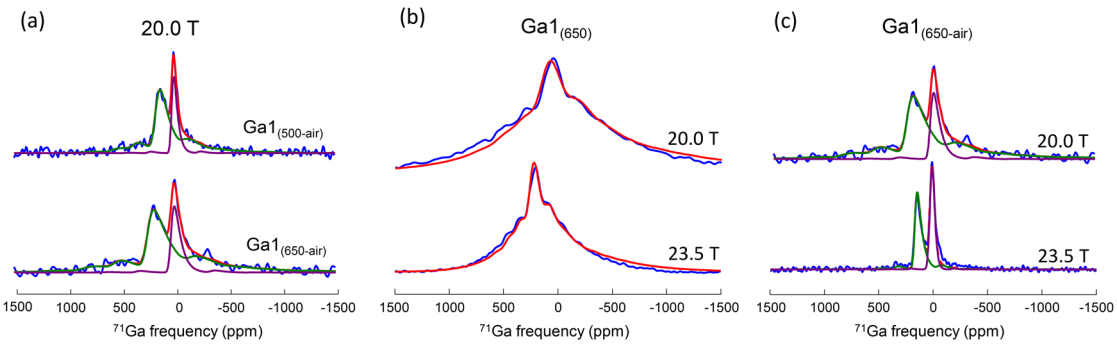

Fig. 2 Experimental ^{71}Ga MAS NMR Carr–Purcell–Meiboom–Gill (CPMG) spectra of (a) $Ga1_{(500\text{-air})}$ and $Ga1_{(650\text{-air})}$ collected at 20.0 T, (b) $Ga1_{(650)}$ and (c) $Ga1_{(650\text{-air})}$ collected at 20.0 T and 23.5 T. The simulation is presented in red, with the individual fitted components shown in purple ($^{[4]}$Ga) and green ($^{[6]}$Ga).

Table 1 ^{71}Ga NMR parameters retrieved from the simulations of the spectra of $Ga1_{(500\text{-air})}$ collected at 20.0 T as well as $Ga1_{(650\text{-air})}$ and $Ga1_{(650)}$ collected at 20.0 T and 23.5 T: relative fraction, average isotropic chemical shift $\bar{\delta}_{iso}$, full width at half maximum of the distribution of δ_{iso} ($\Delta\delta_{iso}$) and variance of the distribution of quadrupolar tensor elements (σ_Q)

Material	Field (T)	Site	Fraction	$\bar{\delta}_{iso}$ (ppm)	$\Delta\delta_{iso}$ (ppm)	σ_Q (MHz)
$Ga1_{(500\text{-air})}$	20.0	$^{[4]}$Ga	75	186	64.3	9.1
		$^{[6]}$Ga	25	30	31.8	4.9
$Ga1_{(650)}$	20.0	$^{[4]}$Ga	100	155	158.9	14.4
	23.5	$^{[4]}$Ga	100	138	105	15.3
$Ga1_{(650\text{-air})}$	20.0	$^{[4]}$Ga	77	180	51.9	9.7
		$^{[6]}$Ga	23	30	29.5	5.3
	23.5	$^{[4]}$Ga	60	180	26.9	8.1
		$^{[6]}$Ga	40	32	31.9	5.1

large distribution $\Delta\delta_{iso}$ of 159 ppm (105 ppm at 23.5 T) and a very large σ_Q of 14.4 MHz (15.3 MHz at 23.5 T). Both the two-component simulation of the spectrum at 20.0 T or the simulation of a spectrum acquired at a higher magnetic field of 23.5 T did not provide a notably improved fit (Fig. 2b). The discrepancy between modelled and experimental data here may be ascribed to the presence of a sizable chemical shift anisotropy (CSA) interaction which is not taken into account by our model.[21] Overall, the presence of a small quantity ($\leq$ *ca.* 10%) of a highly disordered ($\sigma_Q \geq$ *ca.* 20 MHz) additional component cannot be ruled out.

Comparison of the average isotropic chemical shift of $^{[4]}$Ga sites in $Ga1_{(500\text{-air})}$, $Ga1_{(500)}$ and $Ga1_{(650)}$ reveals a reduction of $\bar{\delta}_{iso}$ with the extent of dehydroxylation, *i.e.*, the $\bar{\delta}_{iso}$ of $^{[4]}$Ga sites decreases from 186 ppm in $Ga1_{(500\text{-air})}$ to 176 ppm in $Ga1_{(500)}$ and further to 155 ppm in $Ga1_{(650)}$ (at 20.0 T).[46,47] This change is explained by an increasing substitution of Ga by Si in the second coordination sphere of $^{[4]}$Ga sites, *i.e.*, a transition from a $^{[4]}Ga_{(Ga)}$ to a $^{[4]}Ga_{(Si)}$ local environment.[21,48] Assuming a shift of *ca.* −8.5 ppm per substitution of one Ga atom by one Si atom in the second coordination sphere of Ga,[21] a decrease in the shift by −31 ppm between $Ga1_{(500\text{-air})}$ and $Ga1_{(650)}$ is in agreement with an almost complete transformation from a $^{[4]}Ga_{(4Ga)}$ to a $^{[4]}Ga_{(4Si)}$ local environment. Thus, the interaction between $Ga_xO_y(OH)_z$ and the silica surface increases with the extent of dehydroxylation at increasing temperature. Furthermore, the continuous increase in σ_Q of the $^{[4]}$Ga sites, from 9.1 MHz in $Ga1_{(500\text{-air})}$ to 12.7 MHz in $Ga1_{(500)}$ and ultimately to 14.4 MHz in $Ga1_{(650)}$ indicates an increasing distribution of the $^{[4]}Ga_{(Si)}$ local environments of the amorphous surface gallosilicate species.[31,49]

When $Ga1_{(650)}$ is exposed to air, it forms species that feature a similar spectrum as the Ga species in $Ga1_{(500\text{-air})}$ (Fig. 2a and S13†). More specifically, the spectrum of $Ga1_{(650\text{-air})}$ is also marked by two distinct NMR peaks, *i.e.*, one characterized by a $\bar{\delta}_{iso}$ at 180 ppm (at both 20.0 T and 23.5 T) for $^{[4]}$Ga sites and another at $\bar{\delta}_{iso}$ 30 ppm at 20.0 T (32 ppm at 23.5 T) for $^{[6]}$Ga sites (Fig. 2c, Table 1). This result indicates that the transition between the $Ga_xO_y(OH)_z$ clusters and the highly dispersed $^{[4]}Ga_{(4Si)}$ gallosilicate species is reversible in $Ga1_{(650)}$ and $Ga1_{(500)}$. Lastly, we note that the NMR parameters derived from the fittings of the discussed ^{71}Ga spectra at 20.0 T and at 23.5 T overall agree fairly well (Fig. 2b and c, Table 1).

To summarize, calcination of $Ga1_{(500\text{-air})}$ at 650 °C provides a distribution (likely, associated with a different amount of strain) of $^{[4]}Ga_{(4Si)}$ sites on an amorphous silica surface, whose parameters obtained by the fitting of high field ^{71}Ga MAS NMR spectra are notably similar to that of the SOMC-derived material that contains isolated [(≡SiO)$_3$Ga(XOSi≡)] sites (X is H or ≡Si).[11,38]

Transformation of $Ga1_{(500\text{-air})}$ to $Ga1_{(650)}$ followed by Ga K-edge XAS and FTIR

The changes in the local environment of the Ga sites during dehydration and dehydroxylation were also followed by *in situ* Ga K-edge X-ray absorption near edge structure (XANES) experiments performed during the calcination of $Ga1_{(500\text{-air})}$ (Fig. 3a–c). Here, $Ga1_{(500\text{-air})}$ was placed in a capillary reactor and XANES spectra were recorded *in situ* while heating the material to 650 °C under a flow of synthetic air (10 ml min^{-1}, 5 °C min^{-1}). The temperature of 650 °C was kept for 1 h, followed by the cooling down of the material to 50 °C under 10 ml min^{-1} of N_2. The starting material $Ga1_{(500\text{-air})}$ displays a primary white line feature at *ca.* 10 374.2 eV, which is ascribed to tetracoordinate $^{[4]}$Ga sites.[21,50–52] A further, albeit less pronounced feature at *ca.* 10 377.8 eV is attributed to hexacoordinate $^{[6]}$Ga sites when taking into account the ^{71}Ga MAS NMR results discussed above. Heating of $Ga1_{(500\text{-air})}$ in synthetic air to 650 °C leads to a gradual decrease of the intensity of the feature attributed to $^{[4]}$Ga sites, accompanied by a shift of by *ca.* 0.5 eV, *i.e.* from 10 374.2 eV at 50 °C to 10 373.7 eV at 650 °C (Fig. 3a). Concomitantly, the intensity of the white line feature due to $^{[6]}$Ga sites reduces, while its position remains nearly unchanged at 10 377.8 eV (Fig. 3a). Furthermore, during calcination, the position of the absorption edge (defined as maximum in the derivative plot) shifts notably from 10 372.2 eV at 50 °C to 10 371.2 eV at 650 °C. We hypothesize that these changes in the XANES features are due to the changing coordination environment of Ga and are not related to the decreasing average oxidation state of Ga, which remains Ga^{3+}. The observed changes possibly relate to the evolution of the coordination environment of Ga from $^{[4,6]}Ga_{(Ga)}$ sites in $Ga1_{(500\text{-air})}$ to $^{[4,5]}Ga_{(Ga/Si)}$ in $Ga1_{(500)}$,[21]

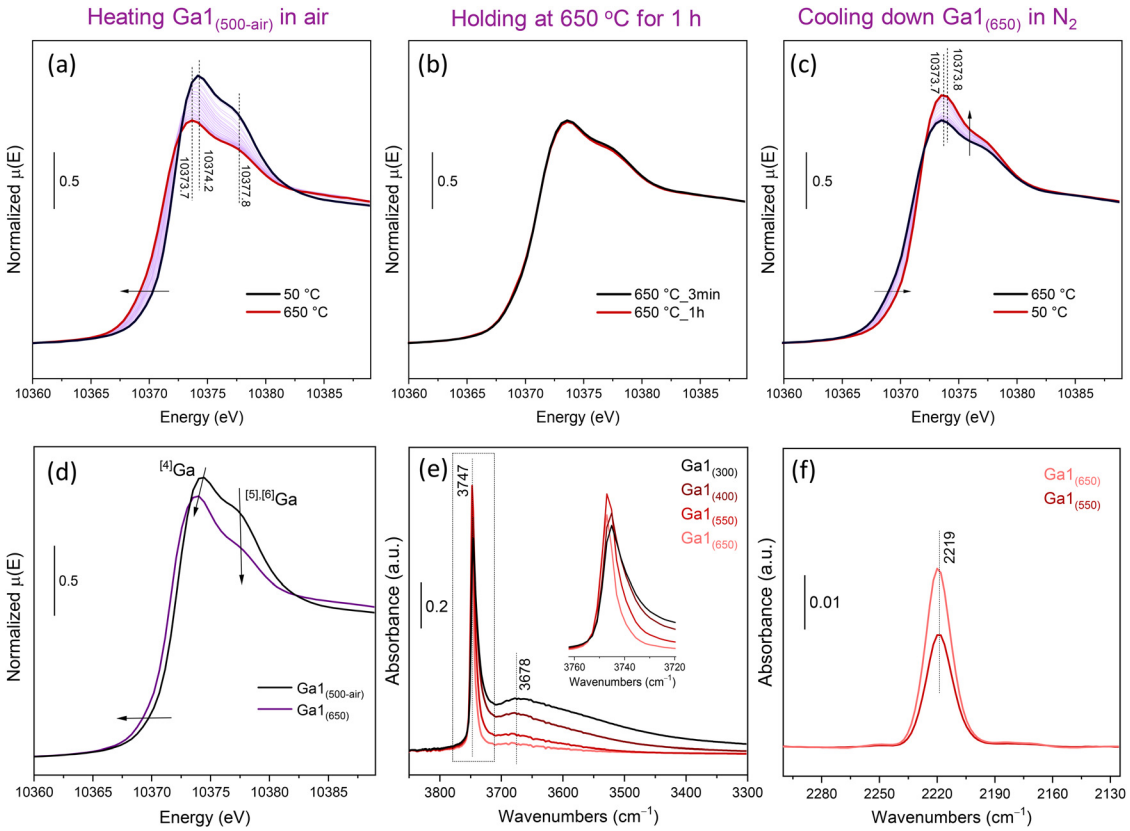

Fig. 3 (a)–(c). *In situ* calcination of $Ga1_{(500\text{-air})}$ followed by Ga K-edge XANES. The arrows indicate the direction of change. (d) XANES spectra of $Ga1_{(500\text{-air})}$ and $Ga1_{(650)}$ as obtained in the *in situ* XANES experiment, recorded at 50 °C. (e) FTIR spectra of $Ga1_{(500\text{-air})}$ in the hydroxyl region (respective evacuation temperatures specified) and, (f) FTIR spectra of $Ga1_{(500\text{-air})}$ after evacuation at 550 °C and 650 °C and CO adsorption at a pressure of 20 Torr at room temperature.

and predominantly $^{[4]}Ga_{(4Si)}$ in $Ga1_{(650)}$.[11,53] It is worth noting that when contrasting the results of our ^{71}Ga MAS NMR and *in situ* Ga K-edge XANES, features of $^{[5]}$Ga and $^{[6]}$Ga sites in the amorphous gallosilicate species studied here could not be resolved in the XANES data.[21]

Furthermore, we do not observe any considerable changes in XANES when holding the material at 650 °C in a flow of synthetic air for 1 h (Fig. 3b). However, during the subsequent cooling down under N_2 (it takes *ca.* 1 h for the specimen to cool down to 50 °C), the edge energy increased from 10 371.2 eV to 10 371.8 eV. Interestingly, also the intensities of the white line features assigned to $^{[4]}$Ga and $^{[5,6]}$Ga sites increased during the cooling down phase, yet to a different extent, with a more pronounced increase observed for the feature assigned to $^{[4]}$Ga sites (Fig. 3c). Specifically, the peak position of the feature assigned to $^{[4]}$Ga sites increased slightly upon cooling down, *i.e.*, from 10 373.7 eV at 650 °C to 10 373.8 eV at 50 °C. The XANES spectra of $Ga1_{(500\text{-air})}$ and $Ga1_{(650)}$ recorded at 50 °C are presented in Fig. 3d. The intensity of the white line feature assigned to $^{[5,6]}$Ga sites significantly decreases after dehydroxylation, while the intensity of the white line features assigned to $^{[4]}$Ga decreases to a lesser extent. Possible explanations for the increase of the edge energy by *ca.* 0.6 eV upon the cooling down of $Ga1_{(650)}$ in N_2 include either a partial re-condensation and dissociation of water on Ga–O–Si linkages, yielding GaOH and SiOH sites (with water formed during the dehydroxylation process or traces of water present in the N_2 flow), and/or increasing the amount of $^{[5,6]}$Ga sites relative to $^{[4]}$Ga sites (note that $^{[6]}$Ga sites in the gallium acetylacetonate reference feature a higher edge energy relative to, for instance, $Ga1_{(500\text{-air})}$, see Fig. S2†).[23]

EXAFS data collected at 50 °C of $Ga1_{(500\text{-air})}$ and $Ga1_{(650)}$, the latter prepared in the *in situ* XAS experiment, are presented in Fig. S3–S5† and the fitting results are summarized in Table 2. The primary feature associated with the first coordination shell, *i.e.*, the Ga–O paths, is present in both materials. While $Ga1_{(500\text{-air})}$ has a fitted Ga–O distance of 1.84(1) Å, a shorter fitted Ga–O distance of 1.82(1) Å is obtained for $Ga1_{(650)}$. Further, the average coordination numbers (CNs) for the first sphere are 5.6(5) in $Ga1_{(500\text{-air})}$ and 4.5(5) in $Ga1_{(650)}$. The decreased distance of the Ga–O path and the lower CN in $Ga1_{(650)}$ suggest that the relative abundance of $^{[4]}$Ga sites increases during the calcination of $Ga1_{(500\text{-air})}$ (as $^{[4]}$Ga sites are expected to feature a lower Ga–O distance compared with $^{[5,6]}$Ga sites). Thus, the results of EXAFS analysis are consistent with the conclusions drawn from XANES and NMR analyses. The second coordination sphere of $Ga1_{(500\text{-air})}$ is modeled with a Ga–Ga path with an average distance of 2.98(6) Å and CN of 4.3(3). In contrast,

Table 2 Best fits of the structural parameters obtained from Ga K-edge EXAFS FT of $Ga1_{(500\text{-air})}$ and $Ga1_{(650)}$

Material	Neighbour	CN	r (Å)	σ_2 (Å^2)	ΔE_0 (eV)	R-Factor
$Ga1_{(500\text{-air})}$	O	5.6(5)	1.84(1)	0.010(1)	−2(1)	0.002
	Ga	4.3(3)	2.98 (6)	0.023(6)		
$Ga1_{(650)}$	O	4.5(5)	1.82(1)	0.010(1)	1(2)	0.002
	Si	0.5(8)	2.76(9)	0.008(8)		
	Ga	1.0(9)	2.84(3)	0.008(8)		

All materials were measured at ambient temperature. S_0 was fixed to 1 as obtained by fitting a β-Ga_2O_3 reference. CN refers to the coordination number, σ^2 refers to the mean squared displacement of the half path length and ΔE_0 refers to edge energy uncertainty.

$Ga1_{(650)}$ was well modeled with both Ga–Si and Ga–Ga paths within its second shell, with distances of 2.76(9) Å and 2.84(3) Å and average CNs of 0.5(8) and 1.0(9), respectively. Note that the Ga–Si and Ga–Ga paths overlap leading to a high uncertainty of the determination in their CNs. The reduced CNs of the Ga–Ga path, in combination with the shortened Ga–Ga distance and the emergence of a Ga–Si path in $Ga1_{(650)}$ are consistent with the transformation of Ga_x-$O_y(OH)_z$ clusters in $Ga1_{(500\text{-air})}$ to highly dispersed gallosilicate species in $Ga1_{(650)}$, that is, predominantly $^{[4]}Ga_{(4Si)}$ sites. The high dispersion of Ga in $Ga1_{(650\text{-air})}$ is shown by EDX mapping (Fig. S8 and S9†). We note, however, that an amorphous GaO_x film with Ga sites in a tetracoordinate environment, that is, with a fitted CN of the first coordination sphere of 3.7(3) has been reported.[54]

To further differentiate between the contributions of Ga–Ga and Ga–Si scattering paths in the second sphere of Ga sites in $Ga1_{(500\text{-air})}$ and $Ga1_{(650)}$, a continuous Cauchy wavelet transform analysis of the EXAFS data was performed.[55] CCWT analysis correlates interatomic distances (r) and wave vector (k) spaces, thereby enabling the distinction between scattering atoms with different atomic numbers located at similar distances from the Ga site. Atoms with higher atomic numbers (such as Ga) scatter more strongly at higher k values than atoms with lower atomic numbers (such as Si). The CCWT analysis of both $Ga1_{(650)}$ and $Ga1_{(500\text{-air})}$ in the R range of 0.5–4 Å reveals a predominant feature due to a Ga–O scattering path and a relatively weak second coordination sphere due to scattering paths from heavier elements (*i.e.*, Ga of Si, see Fig. S6 and S7†). Narrowing the R range to 2–4 Å results, for $Ga1_{(500\text{-air})}$, in two overlapping distinguishable features, *i.e.*, the feature centered at R = 2.4–2.6 Å and k = 8.0–10.0 Å^{-1} attributed to Ga–Ga scattering paths and the feature at R = 2.4–2.6 Å and k = 5.0–7.0 Å^{-1} assigned to scattering from a lighter element, such as O or Si paths (Fig. S6†).[11] In contrast, in the narrow R range of 2–4 Å, $Ga1_{(650)}$ shows distinct features at only R = 2.4–2.6 Å and k = 5.0–7.0 Å^{-1}, attributed to light element scattering (O or Si), while the feature from Ga–Ga scattering paths is not observed (Fig. S7†). This result is consistent with ^{71}Ga NMR results discussed above.

Lastly, to confirm the relationship between the extent of dehydroxylation and amounts of available surface LAS, complementary FTIR experiments of $Ga1_{(500\text{-air})}$ exposed to increasing evacuation temperatures in the range 300–650 °C were performed. Fig. 3e plots the OH vibration region of the acquired spectra that consist of two characteristic features, *i.e.*, a sharp band at 3747 cm^{-1} due to isolated silanols and a broad band centered at *ca.* 3678 cm^{-1} that can be due to both GaOH and Brønsted acidic $^{[4]}Ga_{(Ga/Si)}$–μ^2-OH–Si groups.[56,57] With increasing temperature (from 300 °C to 650 °C) the intensity of the silanol band at 3747 cm^{-1} firstly increases and then decreases (Fig. 3e, inset), explained by a progressive dehydroxylation of the material that leads to a decreased perturbation of isolated silanols, explaining the initial increase of the band at 3747 cm^{-1} (Fig. S11 and S12†). In parallel, also the intensity of the band at 3678 cm^{-1} decreases with increasing temperature; at 650 °C this band has nearly disappeared (Fig. 3e). Overall, the observed decrease of the intensity of both OH bands is due to dehydroxylation.

We have also assessed the effect of dehydroxylation on the density of strong LAS, using CO as a probe molecule. Fig. 3f presents the CO-FTIR spectra of $Ga1_{(550)}$ and $Ga1_{(650)}$. Both spectra display a single band at 2219 cm^{-1}, corresponding to CO coordinated to strong Ga^{3+} LAS.[24,58,59] The intensity of this band increases with increasing temperature and correlates with the disappearance of the broad band in the OH-region at 3678 cm^{-1}; *i.e.* the condensation of hydroxyls with increasing temperature leads to an increasing exposure of Ga^{3+} LAS on the surface of $Ga1_{(650)}$. A control experiment shows that the SOMC-prepared $Ga@SiO_{2(650)}$ material displays the CO band at the same position of 2219 cm^{-1} as $Ga1_{(550)}$ and $Ga1_{(650)}$ (Fig. S10†), suggesting that both materials contain Lewis acidic Ga^{3+} sites of similar strength (and structure). Overall, the portfolio of characterization methods discussed in this study (^{71}Ga MAS NMR, Ga K-edge XANES and EXAFS, Py ^{15}N DNP SENS, Py-FTIR, CO-FTIR, H_2 dissociation followed by FTIR as well as the catalytic properties) do not reveal significant differences between the ALD-derived and SOMC-derived Ga-based silica-supported materials, suggesting that both materials feature predominantly $^{[4]}Ga_{(4Si)}$ sites.

Conclusion

We presented experimental evidence that demonstrates a thermally-induced conversion of silica-supported sub-nanometer $Ga_xO_y(OH)_z$ clusters consisting of $^{[4]}Ga_{(Ga)}$ and $^{[6]}Ga_{(Ga)}$ sites, to a silica surface dominated by isolated $^{[4]}Ga_{(4Si)}$ sites (*i.e.*, surface gallosilicate). Importantly, this process is reversible and exposure of $Ga1_{(650)}$ to ambient air (*i.e.*, rehydroxylation) regenerates the sub-nanometer $Ga_xO_y(OH)_z$ clusters with $^{[4]}Ga_{(Ga)}$ and $^{[6]}Ga_{(Ga)}$

sites. Thus, increasing the dispersion of Ga sites that are likely active in PDH (*i.e.*, $^{[4]}Ga_{(4Si)}$ sites) is a dynamic reversible process that can be achieved through the dehydroxylation of silica containing sub-nanometer $Ga_xO_y(OH)_z$ clusters. The $^{[4]}Ga_{(4Si)}$ coordination environment in the dehydroxylated material is composed of two principal [(≡SiO)$_3$Ga(XOSi≡)] sites, where X is either H (strong BAS) or Si≡ (strong LAS); such sites are also contained in a related material prepared using the SOMC/TMP approach.[11,15,38] The similarity of two materials extends also to a comparable catalytic performance in propane dehydrogenation (high activity and selectivity, low coking and deactivation) as revealed in a 20 h catalytic test. In other words, we provided evidence that ALD methodology can yield well-defined isolated surface gallosilicate sites that closely resemble those prepared *via* SOMC, serving as an example of the complementarity of ALD and SOMC methodologies. The transformation of $^{[4]}Ga_{(Ga)}$ and $^{[6]}Ga_{(Ga)}$ sites to $^{[4]}Ga_{(4Si)}$ sites is similar to the known chemistry of V_2O_5 on hydroxylated SiO_2, which evolves, upon dehydroxylation of silica and at sub-monolayer V coverage, into isolated (≡SiO)$_3$V=O sites.[60–63] The current study highlights the dynamic transformation of surface species under dehydroxylation and re-hydroxylation conditions.

Author contributions

Z. C. and A. F. conceived the research project and designed experiments. Z. C. synthesized and characterized ALD-based materials and analyzed data. A. I. S. conducted FTIR experiments. A. K. performed ICP-OES, STEM and EDX characterization. P. M. A. supervised XAS experiments and XAS data analysis. D. G. and P. F. carried out ^{71}Ga NMR experiments. P. F. performed data analysis of ^{71}Ga NMR experiments. S. R. D. synthesized Ga@SiO_2. A. Y. performed the ^{15}N DNP SENS experiment. C. C. and C. R. M. acquired funding for this project. Data were discussed among all co-authors. Z. C. and A. F. wrote the first draft that was reviewed and edited by all authors. All authors gave their final approval to the final version of the manuscript.

Conflicts of interest

There are no conflicts to declare.

Acknowledgements

This work was supported by ETH Zürich through a doctoral fellowship to Z. C. (ETH-40 17-2). We are grateful to the Scientific Centre for Optical and Electron Microscopy (ScopeM, ETH Zürich) for providing access to electron microscopy facilities. The Swiss Norwegian Beamlines (SNBL) at the European Synchrotron Facilities (ESRF) are acknowledged for providing access to the BM31 beamline. We thank Dr. Dragos Stoian for assistance with X-ray absorption spectroscopy measurements. We thank the Pan-European Solid-State NMR Infrastructure for Chemistry-Enabling Access (PANACEA) program (funding from the European Union's Horizon 2020 research and innovation program under grant agreement 101008500) for provision of the measurement time. This publication was created as a part of NCCR Catalysis (grant agreement no. 819573), a National Centre of Competence in Research funded by the Swiss National Science Foundation.

References

1 J. S. Plotkin, The Changing Dynamics of Olefin Supply/Demand, *Catal. Today*, 2005, **106**, 10–14.
2 H. A. Wittcoff, B. G. Reuben and J. S. Plotkin, *Industrial Organic Chemicals*, John Wiley & Sons, Inc., Hoboken, New Jersey, 2nd edn, 2004.
3 S. R. Docherty, L. Rochlitz, P. A. Payard and C. Copéret, Heterogeneous Alkane Dehydrogenation Catalysts Investigated Via a Surface Organometallic Chemistry Approach, *Chem. Soc. Rev.*, 2021, **50**, 5806–5822.
4 S. Chen, X. Chang, G. Sun, T. Zhang, Y. Xu, Y. Wang, C. Pei and J. Gong, Propane Dehydrogenation: Catalyst Development, New Chemistry, and Emerging Technologies, *Chem. Soc. Rev.*, 2021, **50**, 3315–3354.
5 Z. Nawaz, Light Alkane Dehydrogenation to Light Olefin Technologies: A Comprehensive Review, *Rev. Chem. Eng.*, 2015, **31**, 413–436.
6 B. V. Vora, Development of Dehydrogenation Catalysts and Processes, *Top. Catal.*, 2012, **55**, 1297–1308.
7 N. Raman, M. Wolf, M. Heller, N. Heene-Würl, N. Taccardi, M. Haumann, P. Felfer and P. Wasserscheid, GaPt Supported Catalytically Active Liquid Metal Solution Catalysis for Propane Dehydrogenation–Support Influence and Coking Studies, *ACS Catal.*, 2021, **11**, 13423–13433.
8 K. Searles, K. W. Chan, J. A. Mendes Burak, D. Zemlyanov, O. Safonova and C. Copéret, Highly Productive Propane Dehydrogenation Catalyst Using Silica-Supported Ga–Pt Nanoparticles Generated from Single-Sites, *J. Am. Chem. Soc.*, 2018, **140**, 11674–11679.
9 H. C. Kwon, Y. Park, J. Y. Park, R. Ryoo, H. Shin and M. Choi, Catalytic Interplay of Ga, Pt, and Ce on the Alumina Surface Enabling High Activity, Selectivity, and Stability in Propane Dehydrogenation, *ACS Catal.*, 2021, **11**, 10767–10777.
10 J. J. H. B. Sattler, I. D. Gonzalez-Jimenez, L. Luo, B. A. Stears, A. Malek, D. G. Barton, B. A. Kilos, M. P. Kaminsky, T. W. G. M. Verhoeven, E. J. Koers, M. Baldus and B. M. Weckhuysen, Platinum-Promoted Ga/Al_2O_3 as Highly Active, Selective, and Stable Catalyst for the Dehydrogenation of Propane, *Angew. Chem., Int. Ed.*, 2014, **53**, 9251–9256.
11 K. Searles, G. Siddiqi, O. V. Safonova and C. Copéret, Silica-Supported Isolated Gallium Sites as Highly Active, Selective and Stable Propane Dehydrogenation Catalysts, *Chem. Sci.*, 2017, **8**, 2661–2666.
12 V. J. Cybulskis, S. U. Pradhan, J. J. Lovón-Quintana, A. S. Hock, B. Hu, G. Zhang, W. N. Delgass, F. H. Ribeiro and J. T. Miller, The Nature of the Isolated Gallium Active Center for Propane Dehydrogenation on Ga/SiO_2, *Catal. Lett.*, 2017, **147**, 1252–1262.

13 A. B. Getsoian, U. Das, J. Camacho-Bunquin, G. Zhang, J. R. Gallagher, B. Hu, S. Cheah, J. A. Schaidle, D. A. Ruddy, J. E. Hensley, T. R. Krause, L. A. Curtiss, J. T. Miller and A. S. Hock, Organometallic Model Complexes Elucidate the Active Gallium Species in Alkane Dehydrogenation Catalysts Based on Ligand Effects in Ga K-edge XANES, *Catal. Sci. Technol.*, 2016, **6**, 6339–6353.

14 C. Copéret, F. Allouche, K. W. Chan, M. P. Conley, M. F. Delley, A. Fedorov, I. B. Moroz, V. Mougel, M. Pucino, K. Searles, K. Yamamoto and P. A. Zhizhko, Bridging the Gap between Industrial and Well-Defined Supported Catalysts, *Angew. Chem., Int. Ed.*, 2018, **57**, 6398–6440.

15 C. Copéret, A. Comas-Vives, M. P. Conley, D. P. Estes, A. Fedorov, V. Mougel, H. Nagae, F. Nunez-Zarur and P. A. Zhizhko, Surface Organometallic and Coordination Chemistry toward Single-site Heterogeneous Catalysts: Strategies, Methods, Structures, and Activities, *Chem. Rev.*, 2016, **116**, 323–421.

16 K. L. Fujdala and T. D. Tilley, Design and Synthesis of Heterogeneous Catalysts: The Thermolytic Molecular Precursor Approach, *J. Catal.*, 2003, **216**, 265–275.

17 S. M. George, Atomic Layer Deposition: An Overview, *Chem. Rev.*, 2010, **110**, 111–131.

18 A. R. Mouat, C. George, T. Kobayashi, M. Pruski, R. P. van Duyne, T. J. Marks and P. C. Stair, Highly Dispersed SiO_X/Al_2O_3 Catalysts Illuminate the Reactivity of Isolated Silanol Sites, *Angew. Chem., Int. Ed.*, 2015, **54**, 13346–13351.

19 A. R. Mouat, T. Kobayashi, M. Pruski, T. J. Marks and P. C. Stair, Direct Spectroscopic Evidence for Isolated Silanols in SiO_x/Al_2O_3 and Their Formation Mechanism, *J. Phys. Chem. C*, 2017, **121**, 6060–6064.

20 S. Haukka, E.-L. Lakomaa and T. Suntola, Adsorption Controlled Preparation of Heterogeneous Catalysts, *Stud. Surf. Sci. Catal.*, 1999, **120**, 715–750.

21 Z. Chen, N. K. Zimmerli, M. Zubair, A. V. Yakimov, S. Bjorgvinsdottir, N. Alaniva, E. Willinger, A. B. Barnes, N. M. Bedford, C. Copéret, P. Florian, P. M. Abdala, A. Fedorov and C. R. Müller, Nature of GaO_X Shells Grown on Silica by Atomic Layer Deposition, *Chem. Mater.*, 2023, **35**, 7475–7490.

22 P. Castro-Fernández, D. Mance, C. Liu, P. M. Abdala, E. Willinger, A. A. Rossinelli, A. I. Serykh, E. A. Pidko, C. Copéret, A. Fedorov and C. R. Müller, Bulk and Surface Transformations of Ga_2O_3 Nanoparticle Catalysts for Propane Dehydrogenation Induced by a H_2 Treatment, *J. Catal.*, 2022, **408**, 155–164.

23 P. Castro-Fernández, D. Mance, C. Liu, I. B. Moroz, P. M. Abdala, E. A. Pidko, C. Copéret, A. Fedorov and C. R. Müller, Propane Dehydrogenation on Ga_2O_3-Based Catalysts: Contrasting Performance with Coordination Environment and Acidity of Surface Sites, *ACS Catal.*, 2021, **11**, 907–924.

24 P. Castro-Fernandez, A. I. Serykh, A. V. Yakimov, I. P. Prosvirin, A. V. Bukhtiyarov, P. M. Abdala, C. Coperet, A. Fedorov and C. R. Müller, Atomic-Scale Changes of Silica-supported Catalysts with Nanocrystalline or Amorphous Gallia Phases: Implications of Hydrogen Pretreatment on Their Selectivity for Propane Dehydrogenation, *Catal. Sci. Technol.*, 2022, **12**, 3957–3968.

25 P. Castro-Fernández, M. Kaushik, Z. Wang, D. Mance, E. Kountoupi, E. Willinger, P. M. Abdala, C. Copéret, A. Lesage, A. Fedorov and C. R. Müller, Uncovering Selective and Active Ga Surface Sites in Gallia–Alumina Mixed-Oxide Propane Dehydrogenation Catalysts by Dynamic Nuclear Polarization Surface Enhanced NMR Spectroscopy, *Chem. Sci.*, 2021, **12**, 15273–15283.

26 M. Muoz, F. Farges and P. Argoul, Continuous Cauchy Wavelet Transform of XAFS Spectra, *Phys. Scr.*, 2005, **115**, 221–222.

27 F. H. Larsen, H. J. Jakobsen, P. D. Ellis and N. C. Nielsen, QCPMG-MAS NMR of Half-integer Quadrupolar Nuclei, *J. Magn. Reson.*, 1998, **131**, 144–147.

28 D. Massiot, F. Fayon, M. Capron, I. King, S. Le Calvé, B. Alonso, J. O. Durand, B. Bujoli, Z. Gan and G. Hoatson, Modelling One-and Two-dimensional Solid-state NMR Spectra, *Magn. Reson. Chem.*, 2002, **40**, 70–76.

29 G. Czjzek, J. Fink, F. Götz, H. Schmidt, J. Coey, J.-P. Rebouillat and A. Liénard, Atomic Coordination and the Distribution of Electric Field Gradients in Amorphous Solids, *Phys. Rev. B: Condens. Matter Mater. Phys.*, 1981, **23**, 2513–2530.

30 M. Merko, S. Delsing, G. W. Busser and M. Muhler, Non-oxidative Dehydrogenation of Methanol to Formaldehyde over Supported GaO_x-based Catalysts, *J. Catal.*, 2023, **427**, 115111.

31 C. S. Praveen, A. P. Borosy, C. Copéret and A. Comas-Vives, Strain in Silica-Supported Ga(III) Sites: Neither Too Much nor Too Little for Propane Dehydrogenation Catalytic Activity, *Inorg. Chem.*, 2021, **60**, 6865–6874.

32 E. Parry, An Infrared Study of Pyridine Adsorbed on Acidic Solids. Characterization of Surface Acidity, *J. Catal.*, 1963, **2**, 371–379.

33 I. B. Moroz, K. Larmier, W.-C. Liao and C. Copéret, Discerning γ-Alumina Surface Sites with Nitrogen-15 Dynamic Nuclear Polarization Surface Enhanced NMR Spectroscopy of Adsorbed Pyridine, *J. Phys. Chem. C*, 2018, **122**, 10871–10882.

34 W. Jiang, L. Lumata, W. Chen, S. Zhang, Z. Kovacs, A. D. Sherry and C. Khemtong, Hyperpolarized ^{15}N-Pyridine Derivatives as PH-Sensitive MRI Agents, *Sci. Rep.*, 2015, **5**, 9104–9110.

35 W. R. Gunther, V. K. Michaelis, R. G. Griffin and Y. Roman-Leshkov, Interrogating the Lewis Acidity of Metal Sites in Beta Zeolites with ^{15}N Pyridine Adsorption Coupled with MAS NMR Spectroscopy, *J. Phys. Chem. C*, 2016, **120**, 28533–28544.

36 J. F. Haw, I.-S. Chuang, B. L. Hawkins and G. E. Maciel, Surface Titration of Silica-alumina Monitored by Nitrogen-15 NMR with Cross Polarization and Magic-angle Spinning, *J. Am. Chem. Soc.*, 1983, **105**, 7206–7207.

37 M. Kaushik, C. Leroy, Z. Chen, D. Gajan, E. Willinger, C. R. Müller, F. Fayon, D. Massiot, A. Fedorov, C. Copéret, A. Lesage and P. Florian, Atomic-scale Structure and Its Impact on Chemical Properties of Aluminum Oxide Layers Prepared by Atomic Layer Deposition on Silica, *Chem. Mater.*, 2021, **33**, 3335–3348.

38 S. Docherty, L. Völker, A. Yakimov, R. Verel and C. Copéret, ^{71}Ga NMR Signatures of Lewis and Brønsted Acid Sites in Gallium Silicates Evidenced and Deciphered Upon Interaction with Probe Molecules, *J. Phys. Chem. C*, 2023, DOI: **10.1021/acs.jpcc.3c05638**.

39 J. T. Ash and P. J. Grandinetti, Solid-State NMR Characterization of ^{69}Ga and ^{71}Ga in Crystalline Solids, *Magn. Reson. Chem.*, 2006, **44**, 823–831.

40 S. M. Bradley, R. F. Howe and R. A. Kydd, Correlation between ^{27}Al and ^{71}Ga NMR Chemical Shifts, *Magn. Reson. Chem.*, 1993, **31**, 883–886.

41 D. Massiot, I. Farnan, N. Gautier, D. Trumeau, A. Trokiner and J. P. Coutures, ^{71}Ga and ^{69}Ga Nuclear Magnetic Resonance Study of β-Ga_2O_3: Resolution of Four- and Six-fold Coordinated Ga Sites in Static Conditions, *Solid State Nucl. Magn. Reson.*, 1995, **4**, 241–248.

42 B. Zheng, W. Hua, Y. Yue and Z. Gao, Dehydrogenation of Propane to Propene over Different Polymorphs of Gallium Oxide, *J. Catal.*, 2005, **232**, 143–151.

43 R. Wischert, P. Laurent, C. Copéret, F. Delbecq and P. Sautet, γ-Alumina: The Essential and Unexpected Role of Water for the Structure, Stability, and Reactivity of "Defect" Sites, *J. Am. Chem. Soc.*, 2012, **134**, 14430–14449.

44 E. A. Pidko, R. A. van Santen and E. J. Hensen, Multinuclear Gallium-oxide Cations in High-Silica Zeolites, *Phys. Chem. Chem. Phys.*, 2009, **11**, 2893–2902.

45 S. Yasumura, M. Huang, X. Wu, C. Liu, T. Toyao, Z. Maeno and K.-I. Shimizu, A CHA Zeolite Supported Ga-oxo Cluster for Partial Oxidation of CH_4 at Room Temperature, *Catal. Today*, 2020, **352**, 118–126.

46 H. K. C. Timken and E. Oldfield, Solid-State Gallium-69 and Gallium-71 Nuclear Magnetic Resonance Spectroscopic Studies of Gallium Analog Zeolites and Related Systems, *J. Am. Chem. Soc.*, 1987, **109**, 7669–7673.

47 A. Singh and K. Reddy, Synthesis, Characterization, and Catalytic Activity of Gallosilicate Analogs of Zeolite ZSM-22, *Zeolites*, 1994, **14**, 290–294.

48 A. Arnold, S. Steuernagel, M. Hunger and J. Weitkamp, Insight into the Dry-gel Synthesis of Gallium-rich Zeolite [Ga]Beta, *Microporous Mesoporous Mater.*, 2003, **62**, 97–106.

49 L. Floryan, A. P. Borosy, F. Núñez-Zarur, A. Comas-Vives and C. Copéret, Strain Effect and Dual Initiation Pathway in Cr^{III}/SiO_2 Polymerization Catalysts from Amorphous Periodic Models, *J. Catal.*, 2017, **346**, 50–56.

50 S. Geller, Crystal Structure of β-Ga_2O_3, *J. Chem. Phys.*, 1960, **33**, 676–684.

51 K. Nishi, K. Shimizu, M. Takamatsu, H. Yoshida, A. Satsuma, T. Tanaka, S. Yoshida and T. Hattori, Deconvolution Analysis of Ga K-edge XANES for Quantification of Gallium Coordinations in Oxide Environments, *J. Phys. Chem. B*, 1998, **102**, 10190–10195.

52 C. Prieto, T. Blasco, M. Camblor and J. Pérez-Pariente, Characterization of Ga-substituted Zeolite Beta by X-Ray Absorption Spectroscopy, *J. Mater. Chem.*, 2000, **10**, 1383–1387.

53 R. Bardool, D. P. Dean, H. N. Pham, A. K. Datye, S. Raeissi, M. R. Rahimpour and J. T. Miller, Secondary Reactions of Propylene on Ga/γ-Al_2O_3 Propane Dehydrogenation Catalysts, *J. Catal.*, 2023, **428**, 115201.

54 A. Reis, M. Hanke, O. Bierwagen, A. Trampert, P. Mazzolini and E. Welter, Disorder–order Transition in Ga_2O_3 and Its Solid Solution with In_2O_3 Upon Thermal Annealing, *Phys. Status Solidi B*, 2023, **260**, 2200535.

55 M. Munoz, P. Argoul and F. Farges, Continuous Cauchy Wavelet Transform Analyses of EXAFS Spectra: A Qualitative Approach, *Am. Mineral.*, 2003, **88**, 694–700.

56 M. Garciasanchez, Characterization of Ga/HZSM-5 and Ga/HMOR Synthesized by Chemical Vapor Deposition of Trimethylgallium, *J. Catal.*, 2003, **219**, 352–361.

57 Z. A. Taha, E. W. Deguns, S. Chattopadhyay and S. L. Scott, Formation of Digallium Sites in the Reaction of Trimethylgallium with Silica, *Organometallics*, 2006, **25**, 1891–1899.

58 A. I. Serykh and S. P. Kolesnikov, On the Nature of Gallium Species in Gallium-Modified Mordenite and MFI Zeolites. A Comparative DRIFT Study of Carbon Monoxide Adsorption and Hydrogen Dissociation, *Phys. Chem. Chem. Phys.*, 2011, **13**, 6892–6900.

59 A. Zecchina and C. O. Areán, Diatomic Molecular Probes for Mid-IR Studies of Zeolites, *Chem. Soc. Rev.*, 1996, **25**, 187–197.

60 A. M. Love, C. A. Carrero, A. Chieregato, J. T. Grant, S. Conrad, R. Verel and I. Hermans, Elucidation of Anchoring and Restructuring Steps During Synthesis of Silica-Supported Vanadium Oxide Catalysts, *Chem. Mater.*, 2016, **28**, 5495–5504.

61 X. Gao, S. R. Bare, B. M. Weckhuysen and I. E. Wachs, In Situ Spectroscopic Investigation of Molecular Structures of Highly Dispersed Vanadium Oxide on Silica under Various Conditions, *J. Phys. Chem. B*, 1998, **102**, 10842–10852.

62 S. Xie, E. Iglesia and A. T. Bell, Effects of Hydration and Dehydration on the Structure of Silica-Supported Vanadia Species, *Langmuir*, 2000, **16**, 7162–7167.

63 M. Nadjafi, P. M. Abdala, R. Verel, D. Hosseini, O. V. Safonova, A. Fedorov and C. R. Müller, Reducibility and Dispersion Influence the Activity in Silica-supported Vanadium-based Catalysts for the Oxidative Dehydrogenation of Propane: The Case of Sodium Decavanadate, *ACS Catal.*, 2020, **10**, 2314–2321.

